Materials & Design 128 (2017) 98–111

Contents lists available at ScienceDirect

Materials & Design

journal homepage: www.elsevier.com/locate/matdes

On the evolution of cast microstructures during processing of single crystal Ni-base superalloys using a Bridgman seed technique

P. Hallensleben, H. Schaar, P. Thome, N. Jöns, A. Jafarizadeh, I. Steinbach, G. Eggeler, J. Frenzel*

Institute for Materials (IFM), Interdisciplinary Centre for Advanced Materials Simulations (ICAMS), and Institute of Geology, Mineralogy and Geophysics (GMG), Ruhr University Bochum, 44801 Bochum, Germany

ARTICLE INFO

Keywords:
Crystal growth
Superalloys
Directional solidification
Microstructural evolution
Solidification defects

ABSTRACT

The present work takes a new look at a modified Bridgman process (Bridgman seed technique, BST) for the production of laboratory Ni-base single crystal (SX) superalloy cylinders of 12/120 mm diameter/length. This type of specimen is needed to perform inexpensive parametric studies for the development of new SX and for understanding the evolution of microstructures during SX casting. During melting, the seed partially melts back. The elementary segregation processes cause a certain type of constitutional heating/cooling. Competitive growth eventually establishes a constant average dendrite spacing. In the present work it is documented how this dendrite spacing varies in one cylindrical ingot, and how it scatters when a series of SX ingots is produced. This type of information is scarce. The calculated temperature gradient across the solid/liquid interface (calculated by FEM) is in excellent agreement with predictions from the Kurz-Fisher equation which yields a dendrite spacing based on the experimental withdrawal rate and the microstructurally determined average dendrite spacing. The presence of small angle grain boundaries on cross sections which were taken perpendicular to the solidification direction can be rationalized on the basis of small deviations from the ideal growth directions of individual primary dendrites.

GRAPHICAL ABSTRACT

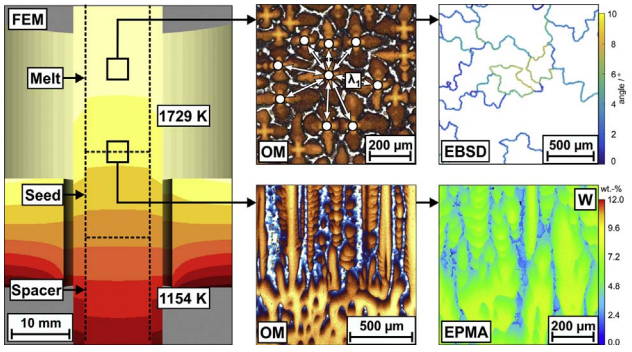

1. Introduction

Ni-base superalloy single crystals (SX) are used to make first stage blades for modern gas turbines which are used in power plants and aero engines, e.g. [1–8]. There are four aspects, which are important and well established: First, SX have no grain boundaries and are therefore less prone to cavitation damage [7,8]. Second, Ni-base superalloys feature chemical and microstructural heterogeneities which have their origin in the solidification process (prior dendritic and interdendritic regions [9], largescale heterogeneity: several hundred micrometers) and in the

* Corresponding author.
E-mail address: jan.a.frenzel@rub.de (J. Frenzel).

http://dx.doi.org/10.1016/j.matdes.2017.05.001
Received 23 February 2017; Received in revised form 11 April 2017; Accepted 1 May 2017
Available online 02 May 2017

subsequent precipitation heat treatment (γ/γ′-microstructure, small scale heterogeneity: 1 μm). Superalloy SX represent technical single crystals which contain two phases, the ordered γ′-phase ($L1_2$ crystal structure, cuboidal particles of a typical edge length of a few hundred nanometers, typical volume fraction of 75%) and the γ-phase (fcc solid solution, thin channels which separate the γ′-cubes, typical volume fraction: 25%). The < 001 > direction represents a natural solidification direction, but deviations of up to 15° from this solidification direction are not uncommon [3,6,10]. Third, Ni-base SX show elastic anisotropy, where the Young's modulus in the < 111 > direction is significantly larger than in the < 001 > direction, e.g. [11,12]. Orienting turbine blades along the < 001 > direction minimizes thermal stresses associated with fast heating and cooling. Fourth, superalloy SX are produced using the well-known Bridgman directional solidification process [1–3,5–8,13]. A detailed overview on industrial scale production of SX turbine blades was recently given by Kubiak et al. [13]. Two different techniques are applied to eliminate grain boundaries in superalloys during directional solidification (DS). First, one can use a narrow spiral-shaped crystal selector through which the solid/liquid front must pass during solidification. The selector only allows one single grain to pass through. The second option is to use pre-oriented seed crystals. The seed partially melts back in the early processing stages. Later, epitaxial growth during crucible withdrawal results in the formation of a solid/liquid interface which proceeds through the molten material.

The processing of SX has been a research topic for several decades [13–16]. A first summary of techniques has been given in the seminal collection of research papers edited by Gilman in 1963 [14]. The research area has always been closely related to the field of solidification of melts [17–21]. As gas turbine technology developed, the casting and the directional solidification of SX superalloys have received considerable attention, e.g. [6,10,22–26]. However, the production of high quality superalloy single crystals has remained challenging [25,26]. The formation of microstructures in Ni-base superalloys during SX solidification is governed by various thermodynamic, kinetic and other constraints and involves different length scales [9,27,28]. The governing elementary processes are more complex than what is envisaged in classical crystallization theories, e.g. [29,30]. High contents of refractory elements (e.g. Re, W and Ta) promote segregation during solidification, which results in heterogeneous microstructures. Even when solidification conditions are precisely controlled, there is a risk of defect formation [6,7,25,26,28].

Today there is a good understanding of the coupling between thermodynamic driving forces and elementary kinetic processes during SX solidification, e.g. [22,31–33]. Progress has been made in the area of process modeling, e.g. [26,34–38]. However, there are open questions related to microstructural and chemical homogeneity across length scales which the present work addresses in four points. First, it is shown how microstructures and local chemical alloy compositions evolve during different stages of a seeded Bridgman solidification process with special emphasis placed on the early stages of partial seed remelting and crystal growth. Second, an effort was made to demonstrate that finite element based calculational procedures can predict temperature gradients in the solid/liquid region which agree well with experimental data derived from primary dendrite arm spacings. Third, it is important to explain the nature of internal interfaces which are inherent features of cast microstructures and which evolve during solidification. Fourth, there is a need to evaluate the extent of microstructural scatter which is observed when a series of single crystals is produced following the same procedure. All findings are discussed in the light of previous results reported in the literature.

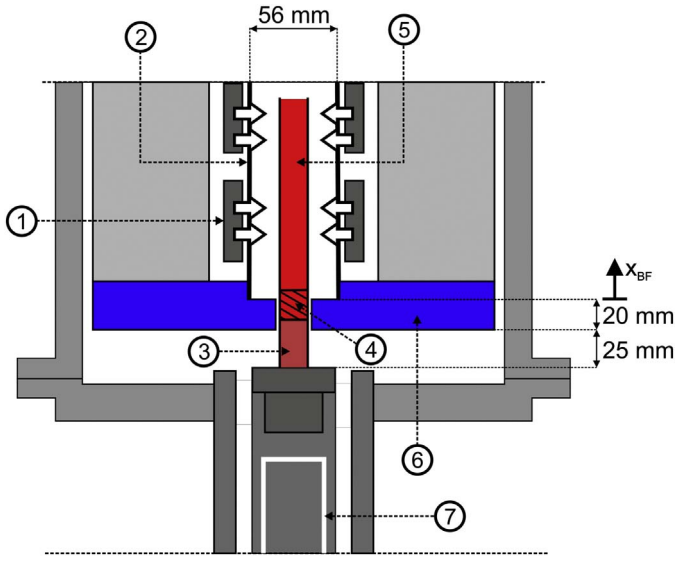

Fig. 1. Key elements of the Bridgman seeding technique (BST) used in the present work: 1 - graphite heaters, 2 - graphite tube, 3 - spacer, 4 - seed, 5 - feedstock, 6 - baffle, 7 - cooled crucible holder. For details see text.

Table 1
Geometries of the seed, the melting feedstock, the alumina tube and the baffle.

Seed	
Diameter	11.6 mm
Length	16 mm
Melting feedstock	
Diameter	11.6 mm
Length	110 mm
Al_2O_3 tube	
Inner diameter	12 mm
Wall thickness	2 mm
Length	180 mm
Roughness	0.1 μm
Baffle	
Thickness (effective)	20 mm
Hole diameter	18 mm

2. Experimental methods

2.1. Bridgman seed technique (BST)

In the present work we use a Bridgman furnace of type KZV-A40-400/161G-V from Gero GmbH (Neuhausen, Germany). The lower part of the furnace is shown in Fig. 1. The furnace has three separately controlled graphite heating elements (one of which is highlighted with "1"). These heat a central graphite tube ("2") which houses the cylindrical crucible, shown in red in Fig. 1. The crucible contains the spacer ("3"), the seed ("4") and the feedstock ("5"). During solidification, the crucible/holder assembly remains in position while the furnace moves upwards. An isolating baffle (shown in blue, "6") separates hot (inside of furnace) and cold (outside of furnace) zones. The crucible holder ("7") is positioned within a water-cooled cylinder. The heaters and graphite tube are thermally isolated by a graphite felt insulation, light grey in Fig. 1. The temperatures in the center of the heated zone are monitored. Prior to melting and directional solidification, the whole melting chamber is evacuated using a rotary vane pump (Pfeiffer DuoLine) and a turbo pump (type Pfeiffer HiPace 400). Spacer, seed crystal and feed stock consist of the superalloy ERBO/1C, a CMSX-4 type of material which has been described in the literature [9].

Table 2
Alloy composition (chemical analysis data provided by supplier).

Element	Al	Co	Cr	Hf	Mo	Re	Ta	Ti	W	Ni
Concentration (wt%)	5.7	9.6	6.5	0.1	0.6	2.9	6.5	1.0	6.4	Bal.

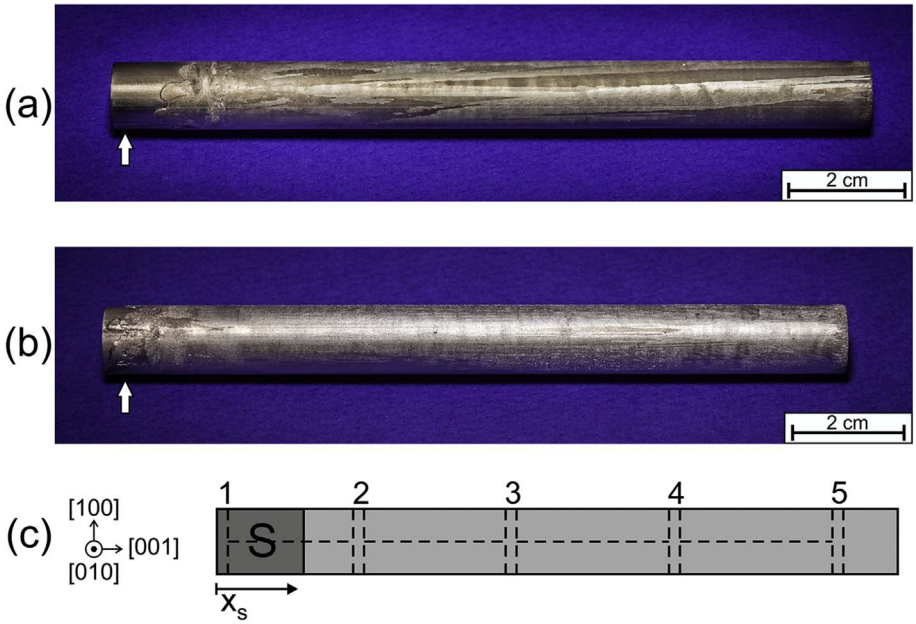

Fig. 2. As-grown Ni-base superalloy cylinders (growth direction < 001 > : from left to right). (a) Directionally solidified (DS) structure with elongated grains. (b) Single crystal (SX) structure obtained using our BST method (seed region highlighted by white arrow). (c) Cut up plan for metallographic sectioning.

Cylindrical ERBO/1C seeds are used as starter crystals (full diameter seeding [39]). Critical geometry and material parameters of the seed, the spacer, the feedstock, the alumina tube and the baffle are given in Table 1. The seeds were cut by electro discharge machining (EDM) from ERBO/1C slabs. Prior to EDM, the slabs were precisely oriented using the Laue method, to ensure that the [001] direction is parallel to the longitudinal axis of the cylindrical seed. Details on our iterative EDM/Laue procedure are given elsewhere [40]. For the experiments performed in the present work, the melting feedstock was specifically prepared by arc melting of ERBO/1C and subsequent drop casting into a cylindrical Cu-mold as described in [41,42]. The alloy used in the present study (for spacer, seed and feedstock) was obtained from Alcoa Howmet (Whitehall, USA). The chemical composition of the alloy is given in Table 2.

Cylindrical Al_2O_3 tubes with low surface roughness were used as crucibles. The tubes were purchased from CeramTec GmbH (Marktredwitz, Germany). Prior to crystal growth, the inner surfaces were cleaned with a brush and pressurized air. Using a special support system, the tubes were mounted onto a crucible holder. The tube was precisely aligned by means of a support frame and mounted onto a crucible holder, where it was fixed using a ceramic glue of type FiberPlast C 1800 D from M.E. Schupp High Temperature Technology (Aachen, Germany). During the drying process, the crucible tube remained fixed in the support frame which minimizes angular deviations. A low oxygen partial pressure was established in the furnace by evacuating and backfilling with Argon (purity 99.995 vol%) for 2 times. Then, the furnace was heated under vacuum to 400 °C. The system was evacuated for at least 10 h until a vacuum level of $1{\cdot}10^{-5}$ mbar was established. Then, the furnace was heated to the target temperature of 1550 °C at a rate of 12 K/min. When the target temperature was reached, a 30 min hold resulted in melting of the feedstock and partial melting of the upper region of the seed crystal. Crystal growth experiments were then carried out at a withdrawal rate of 180 mm/h [28,43]. Fig. 2 shows ingots which were produced and investigated in the present study. The crystals have a length of 120 mm and diameter of 12 mm, the targeted growth direction is < 001 > . Fig. 2a shows a directionally solidified polycrystalline sample, which resulted from an early solidification experiment where the selected process parameters failed to achieve partial seed melting. After adjusting the position of the seed crystal (5 mm above the baffle), a high quality SX specimen was obtained, Fig. 2b. For later reference, Fig. 2c shows the crystallographic reference system and identifies specific regions along the cylindrical sample characterized by the space coordinate x_S. For metallographic investigations, longitudinal and cross sectional cuts were prepared from the locations indicated by dashed lines.

2.2. Sample characterization

The crystallographic orientations of both, seeds (prior to melting) and single crystals (after BST processing) were characterized using a Laue system of type MWL120 with a W cathode operating at 21 kV and 21 mA. Fig. 3 documents our orientation procedure. Fig. 3a shows a Laue pattern from a seed. We additionally use an optical technique where the (secondary) crystal orientation is determined accounting for the orientation of secondary dendrites. Free-standing dendrites can be easily observed in the upper parts of as-grown crystals, with no need for additional metallographic preparation. Fig. 3b shows a sample (“1”) in an optical stereo microscope (“2”) of type Leica MZ 95 which allows to visualize dendrites. The sample is fixed into a steel tube, Fig. 3c, which can rotate around its longitudinal axis (Figs. 3d and e) to define precise cutting directions, Fig. 3f.

The as-cast SX ingots were macro etched to contrast surface grains and related defects, using a solution consisting of 40 ml H_2O, 20 ml HCl and 10 ml H_2O_2. Examples of two etched ingots are shown in Fig. 2. Samples for metallographic characterization were cut from the as-grown crystals using a high precision cutting machine of type Struers Secotom-10. Specimen surfaces were prepared by conventional grinding and polishing procedures. The final polishing step was performed using a 1 μm diamond suspension. An etching solution consisting of 100 ml H_20, 100 ml HCl, 100 ml HNO_3, 3 g MoO_3 was finally applied to establish good contrast. After etching, it was straightforward to visualize grain orientations, to distinguish between different regions of the cast microstructure (dendritic and interdendritic regions) and to identify large γ′ particles. The as grown microstructure was investigated using optical microscopy (OM), scanning electron microscopy (SEM), and chemical microanalysis. An OM of type Zeiss Axio was used to characterize dendrite structures. An effort was made to determine the evolution of average primary dendrite spacings across the crystal length using the procedure outlined in [9]. At least 100 spacings of neighboring dendrites were determined for each sample, with the exception of the seed material where dendrites were widely spaced and where one

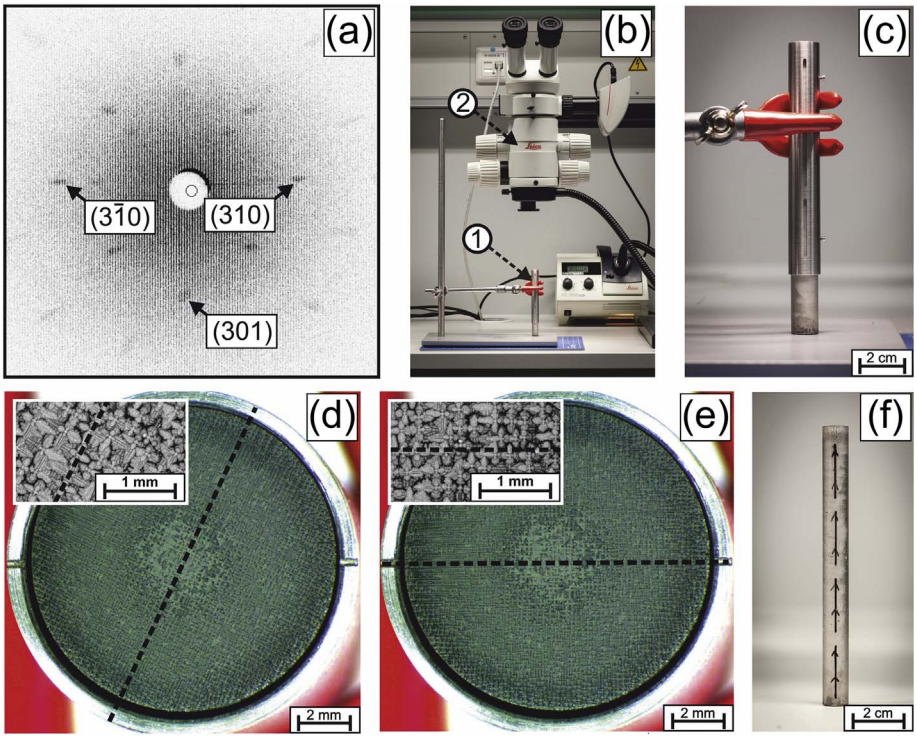

Fig. 3. Orienting SX samples. (a) Laue diffraction patterns obtained from an ERBO seed. (b) Optical method to orient secondary dendrites (as-gown sample "1" is positioned below a stereo microscope "2" to identify the orientations of secondary dendrites). (c) Cylindrical steel holder with several slits which allow to apply markers. (from d to e) The sample is rotated such that secondary dendrite arms are aligned vertically/horizontally. (f) End result: Specimen oriented with respect to primary and secondary dendrites.

therefore could only consider smaller dendrite numbers.

A field-emission electron microprobe (EPMA) of type Cameca SXFiveFE was used to obtain small scale chemical distribution maps of all alloy components. The instrument was operated at an acceleration voltage of 20 kV and a probe current close to 75 nA. Quantitative EPMA data sets were obtained by acquiring both peak and background data and performing a matrix correction (X-Phi procedure [44]) using intensity data of appropriate reference materials. The dimension of each element map was 2048 × 1536 pixel. The pixel step size was 0.5 μm and the dwell time per pixel was 150 ms. Three neighboring sample regions were mapped with a horizontal overlap of 50 μm, which allowed for subsequent merging of the datasets. Depending on their atomic numbers, either Kα, Lα or Mα X-ray lines of the elements were detected, except for Re, where the Mβ line was measured simultaneously on two wavelength-dispersive spectrometers. The large scale chemical homogeneity of the as-grown SX ingots was evaluated using a SEM of type Tescan MIRA3 equipped with an energy dispersive X-ray analysis (EDX) detector of type Oxford X-Max^N. The microscope operated at 20 kV where EDX spectra were recorded within 4 min. For each chemical analysis, an area of 7.3 mm^2 was considered. A SEM of type FEI Quanta FEG 650 equipped with an electron backscatter diffraction (EBSD) camera of type EDAX Ametek Hikari was used to investigate microstructures (20 kV) and to perform orientation imaging SEM (30 kV). A step size of 3.3 μm was selected for EBSD scans. Appropriate grain reconstructions were used in EBSD data processing, which were embedded in the software package MTEX [45,46]. EBSD data analysis allowed to determine the misorientations between the targeted [001] direction and the resulting sample orientations. An effort was made to characterize misorientation angles (axis/angle pair rotation [47]) of low angle grain boundaries (LAGBs). A minimum angle of 0.5° was set for the identification of grain boundaries. In the present work five SX ingots (1–5) were produced, none of which showed macroscopically noticeable defects. Microstructural parameters of all five ingots were determined. All micrographs shown in the present work were obtained from ingot 1.

2.3. Calculation of temperature distribution in the furnace

An effort was made to calculate the temperature distribution which characterizes our BST process. For this purpose the whole furnace/crucible setup was modeled using the finite element (FEM) software package Wincast Expert from RWP GmbH in Aachen, Germany (for details see: [48]). In Fig. 4 we show the part of the FE model which contains the crucible holder, the baffle, the crucible, the feedstock (for thermal analysis no difference was made between spaceholder, seed crystal and melt feedstock), the graphite tube and the heater elements. Fig. 4b and c show how the system was geometrically meshed. Fig. 4c shows the region marked with a horizontal arrow pointing to the left in Fig. 4b at a higher magnification. In fact to properly account for the temperature distribution in our BST process we need to consider a large model which consists of 164 layers and 3,8·10^6 nodes which define 7,6·10^6 cells. For the calculations we need as input the heat conductivities, the heat capacities and the emissivities of the related materials which were taken from the literature [49–51] or from data sheets provided by component manufacturers [52]. Some key parameters used for our calculations are listed in Table 3.

3. Results

3.1. Calculated temperature profile across solid/liquid interface

In Fig. 5 we present results for the temperature distribution in the furnace. In Fig. 5a, temperature levels are represented by colors (see corresponding color code on the right). The horizontal dotted lines in the center of the figure represent calculated isotherms for 1653 and 1593 K, which correspond to the liquidus and solidus temperatures of our alloy, as experimentally determined by Quested et al. [49]. In Fig. 5b we show the calculated temperature profile along the dashed central vertical line. The coordinate along this line was introduced as x_{BF} in Fig. 1, position x_{BF} = 0 corresponding to the upper limit of the baffle. In addition to the calculated T(x_{BF})-profile, Fig. 5b highlights the

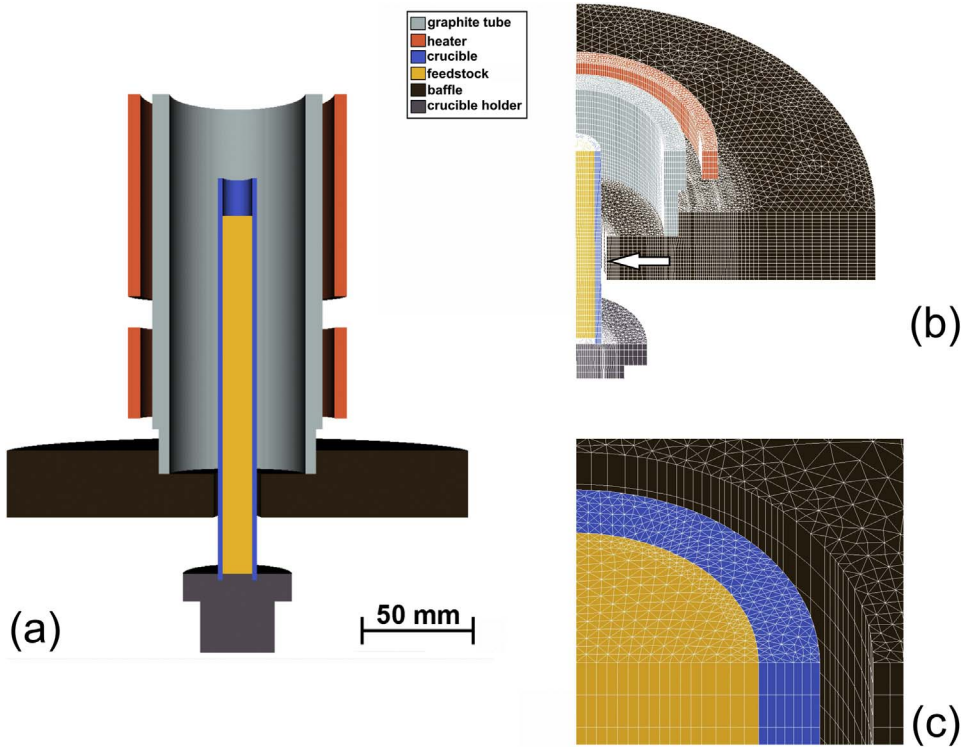

Fig. 4. Illustration of parts of the FEM model which was used to calculate temperature distributions in the Bridgman furnace. (a) Lower part of the Bridgman furnace. (b) Details of FEM mesh in the crucible, crucible holder, feedstock, baffle, graphite tube and lower heater. (c) Details of the FEM mesh at the position of the horizontal arrow in Fig. 4b.

Table 3
Input data used for numerical simulation in the present study. For brevity, only minimum and maximum values of each data set are listed.

	Heat conductivity/W/(cmK)	Heat capacity/J/(cm^3K)	Emissivity
Heater/tube (Graphite)	4 Datapoints [52]	9 Datapoints [52]	0.75 [52]
	293 K: 0.85 (min) 1673 K: 0.40 (max)	473 K: 1.9116 (min) 1873 K: 3.6108 (max)	
Ceramic crucible (Al_2O_3)	16 Datapoints [52]	8 Datapoints [50]	0.9 [52]
	373 K: 0.1722 (min) 1823 K: 0.0407 (max)	473 K: 4.0201 (min) 1873 K: 5.24 (max)	
Feedstock (CMSX-4)	6 Datapoints [49]	8 Datapoints [49]	–
	400 K: 0.09 (min) 1700 K: 0.25 (max)	298 K: 3.4539 (min) 1700 K: 4.8573 (max)	
Crucible holder (Stainless steel)	6 Datapoints [52]	5 Datapoints [52]	0.2 [52]
	293 K: 0.15 (min) 1073 K: 0.251 (max)	293 K: 3.965 (min) 1073 K: 4.9959 (max)	
Baffle (Graphite felt)	10 Datapoints [52]	16 Datapoints [51]	0.95 [52]
	296 K: 0.00116 (min) 1873 K: 0.0094 (max)	373 K: 0.115947 (min) 1873 K: 0.979947 (max)	

liquidus (small red circle) and the solidus temperatures (small blue circle) as reported in [49]. A linear fit of the calculated data between T_L and T_S yields a temperature gradient of 13.9 K/mm.

3.2. Microstructure evolution across the seed/new grown crystal interface

Fig. 6 shows optical micrographs which allow to appreciate how the microstructure changes as we move from the seed on the left of Fig. 6a along the horizontal [001] solidification direction to the right towards the newly grown single crystal. The primary dendrites grow along the natural [001] solidification direction, e.g. [3,24,53]. Primary dendrite spacings are larger in the seed crystal than in the new crystal. A white vertical dashed line in the right part of Fig. 6a indicates the position of the original seed tip. The region between this vertical dashed line and the bright yellow transition zone close to the center of Fig. 6a represents the melt-back zone. This region extends over approximately 6 mm. Fig. 6b shows the dendritic structure of the seed prior to melting. Fig. 6c shows the seed region highlighted by the rectangular field 1 in Fig. 6a. This region did not melt during processing, however, it was exposed to a temperature close to the solidus temperature. A comparison with Fig. 6b shows that this exposure causes microstructural changes. The bright yellow zones in Fig. 6b represent large γ′ particles located in interdendritic regions which shrink during high temperature exposure, Fig. 6c. Fig. 6d shows the microstructure of field 2 from Fig. 6a. Fig. 6d shows a seed region, which underwent partial melting. Its microstructure appears blurred and no longer features the distinct dendritic patterns which characterize Figs. 6b and c. Two bright horizontal bands extending along the [001] solidification direction are marked by white arrows in Fig. 6d. They represent former interdendritic regions which underwent partial melting. The microstructure represents a prior mushy zone region after solidification. Fig. 6e shows the dendritic structure of the newly grown SX, as observed in field 3 of Fig. 6a. No grain boundaries are found in this region and most primary dendrite arms are parallel and well aligned along [001]. Comparing Fig. 6b and e shows that the dendrites in the newly grown crystal exhibit smaller primary dendrite arm spacings than in the seed material.

Fig. 7 shows EPMA results which provide information on element partitioning in the zone where the seed partly melts. The vertical dashed line on the right of Fig. 7a (same position as indicated by the central black dashed line in Fig. 6a) separates the partially melted seed (left of dashed line) from the newly formed crystal. Fig. 7a shows the partitioning of Re between prior dendritic and interdendritic regions (200–700 μm). Close to the dashed line, Re is seen to partition towards

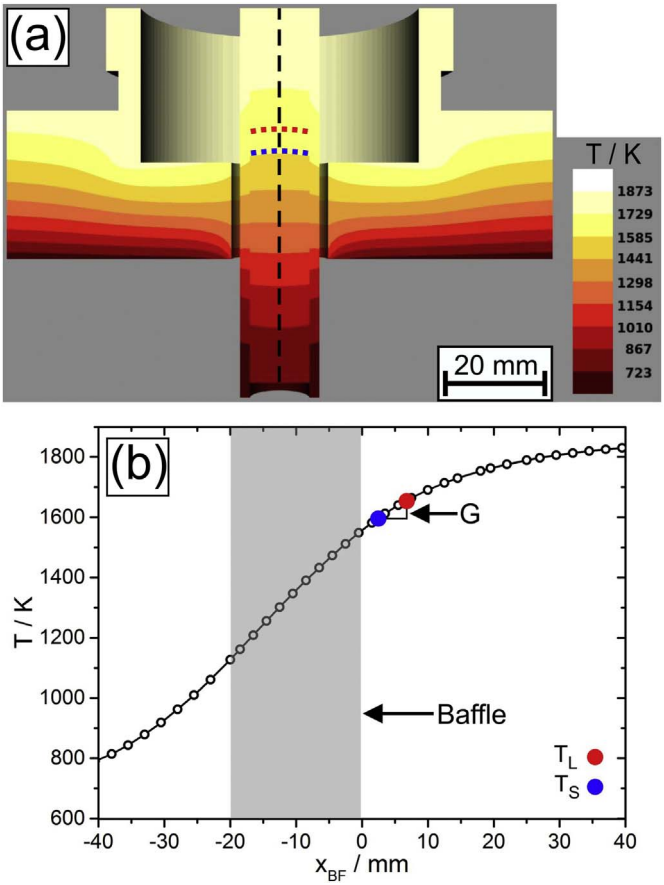

Fig. 5. Temperature distribution during solidification. (a) Color-coded representation of temperature distributions in the lower part of the Bridgman furnace. The dotted red and blue lines represent isotherms which corresponds to T_S and T_L [49], respectively. The dashed vertical line represents a central reference line (for details see text). (b) Temperature profiles along the central dashed reference line in Fig. 5a.

prior dendritic regions of the seed crystal (green contrast). Fig. 7b shows integral concentration results which represent average values obtained from rectangular fields like the one shown on the left of Fig. 7a. Fig. 7b presents the corresponding concentration profiles for W, Ta, Al and Re in the region where the seed underwent partial remelting. As can be seen from Fig. 7b, the concentrations of the elements W and Re (with a distribution coefficient $k' > 1$, [9,23,54]) increase as we approach the dashed line (indicated by little blue arrows pointing up). In contrast, the concentrations of Ta and Al ($k' < 1$, [9,23,54]) decrease (indicated by little blue arrows pointing down). The effects are small but significant and represent direct chemical evidence for interdiffusion processes on the mm-scale which accompany the melting and re-solidification of parts of the seed crystal. Fig. 7c and d show chemical distribution maps from the quadratic region which is highlighted in Fig. 7a. The dark blue regions in Fig. 7c and d indicate low Cr and W concentrations. These regions represent large primary γ′-phase particles. Fig. 7c suggests, that the large γ′ particles are surrounded by a Cr-rich zone.

We now take a closer look at the microstructure between the prior mushy zone and the newly grown crystal, Fig. 8. The left part of Fig. 8a represents the partially remelted seed crystal, on the right we see the newly grown SX. The horizontal arrows in Fig. 8a point to small protrusions. Not all new crystals which form on the seed evolve into large primary dendrites. Instead, some dendrites outgrow others. White arrows in Fig. 8b and c highlight dendrites which underwent some growth before they were outgrown by competing dendrites. The white arrow in Fig. 8b points to a rarely observed [001] tertiary dendrite arm which forms too late to be able to compete with the primary [001] dendrites. In Fig. 8c, one large dendrite has split into two. Thereafter, the lower part of the split dendrite took over and suppressed the growth of its competing co-dendrite.

3.3. Dendrite spacings

In Fig. 9 we take a look at the dendritic microstructure after casting. Fig. 9a shows a SEM micrograph which was obtained from the upper end of an as-grown SX cylinder where free standing dendrites can be seen without further metallographic preparation. The view direction of Fig. 9a is [00-1]. Four secondary arms emanate from the central primary dendrite, which show a fourfold symmetry. A small black arrow marks the beginning of the formation of a tertiary dendrite, which has not grown to a significant length. Fig. 9a suggests that the primary dendrite spacing is close to 200 μm. Fig. 9b shows a lower magnification optical micrograph from a perpendicular cross section of the as-grown crystal. A statistically relevant number of primary dendrites can be clearly distinguished. The small inset in Fig. 9b shows a central dendrite D_C together with seven direct neighbors, numbered from 1 to 7. Fig. 9c shows how dendrite spacings change along the position of a cylindrical bar as illustrated in Fig. 2c. We compare two materials states, where the melt was held for 30 (empty circles) and 90 min (full square symbols) at 1550 °C before the furnace was moved up. For both conditions, a complete melting of the seed crystal could be avoided while a good contact between seed and feedstock was established. Both thermal pre-exposures yielded similar dendrite spacings, Fig. 9c. The primary dendrite spacings in the seed are of the order of 400 μm. In the newly formed SX, average dendrite spacings are close to 200 μm. Dendrite spacings are distributed quantities and typical distributions at different x_s positions along the longitudinal axis of the cylindrical SX bar are shown in Fig. 9d, e and f. It can be seen that the dendrite spacings in the seed crystal (lower number of dendrites) show a wider distribution (ranging from 250 to 712 μm) than in the new SX (ranging from 54 to 348 μm), Figs. 9d and e. Moreover, the dendrite spacing distributions do not change significantly as we move from $x_S = 27$ mm (where solidification started) to $x_S = 114$ mm (close to the end of newly formed SX), Fig. 9e and f.

In Fig. 10 we present results for average values from five dendrite spacing measurements which were performed on five SX cylinders at bar position $x_S = 56$ mm (middle of bar). About 100 measurements were performed for each of the five SX bars: The results are presented in Fig. 10 together with the corresponding standard deviations. From Fig. 10 one can conclude that our Bridgman process yields reproducible primary dendrite spacings. The average spacing of the five ingots is 205 μm.

3.4. Chemical homogeneity

Fig. 11 shows how the alloy chemistry changes as a function of the location in the cylindrical bars. In Fig. 11a we move along the central cylindrical bar axis using x_S as defined in Fig. 2c to indicate the longitudinal position in the bar. Our SEM EDX results suggest that there is no significant change in alloy composition as we move in the longitudinal direction along the bar. In Fig. 11b we consider whether alloy compositions change when we move away from the cross section center of the bar. For this purpose, chemical compositions were measured at five cross-sectional locations as indicated in the light grey circle at the lower right of Fig. 11b. The data in Fig. 11b were obtained for the central position 3 at a longitudinal x_S coordinate of 56 mm, see Fig. 2c. The distances between the positions a, b, c, d and e were of the order of 1 mm. The results shown in Fig. 11b suggest that the chemical composition of our cylindrical bars does not vary in the circular cross section of the bar.

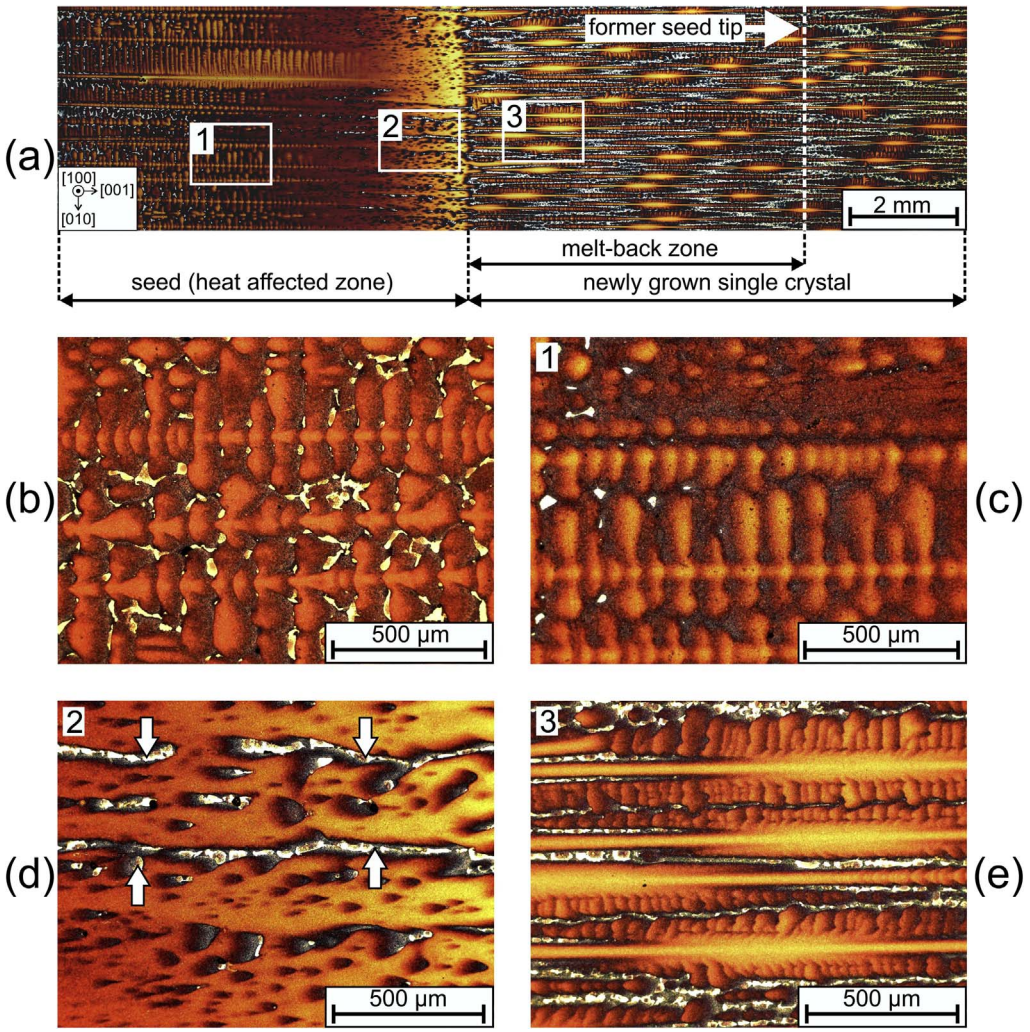

Fig. 6. Evolution of microstructures during BST processing. (a) Overview (growth direction: from left to right). On the left: seed material. Right part: newly grown crystal. White dashed line: position of prior seed tip. (b) Initial microstructure of seed material prior to melting. (c) Heat affected zone in seed material after processing. (d) Partially remelted zone in the seed. Arrows highlight band-like prior interdendritic regions. (e) Fine dendritic microstructure in the newly grown superalloy single crystal.

3.5. Formation of crystal defects

Fig. 12 shows two misoriented regions which were only found in one of the five SX bars. Fig. 12a and b represent optical and orientation imaging SEM micrographs, respectively. Fig. 12b represents a colored coded image, where different crystallographic directions that are parallel to the sample surface normal are represented by different colors as documented in the standard triangle (inset of Fig. 12b). Fig. 12b shows that most of the analyzed crystal region (appearing in red) is oriented in the targeted [100] direction. However, there are two regions where new grains have formed which differ in orientation and appear in orange (misorientation angle: 11°) and blue color (misorientation angle: 35°). These regions were found in only one of the five SX bars. They were located in the melt back zone of the seed close to the mushy zone of the seed.

While new misoriented small grains like those shown in Fig. 12 are rarely observed, a finer scale mosaicity is a common feature of cast SX. Darwin [55] has introduced the term mosaicity as a measure of the spread of crystal orientations, assuming that a mosaic crystal represents an idealized model of an imperfect crystal, which one can imagine to consist of many crystallites which are to some extent randomly misoriented [55]. In the present work we refer to these regions as subgrains and to their boundaries as low angle grain boundaries (LAGBs). Fig. 13 compiles results from SEM and OM investigations which show mosaicity in one of our SX crystals. Fig. 13a shows a cross section of a SX bar at position x_S = 27 mm. The cross section was taken perpendicular to the [001] solidification direction. The figure presents results from orientation imaging SEM and shows a color-coded orientation distribution superimposed over an image quality map. In Fig. 13a we cannot distinguish between primary dendrites. But one can clearly see different regions or subgrains, which are all slightly misoriented from [001]. The inset in Fig. 13a shows a standard triangle which specifies the color coding, where a precise [001] direction corresponds to red. Increasing levels of green or blue in the basic red color tone in subgrains, indicate orientation deviations towards [101] and [111], respectively. Fig. 13b presents the same region as shown in Fig. 13a, two distinct features are highlighted by arrows in both images. Fig. 13b does not show the orientations between different subgrains. Instead it shows all LAGBs, which are color-coded as indicated, to document the degree of misorientation. As can be seen in Fig. 13b, most of the LAGB misorientations are close to 2°. They hardly ever reach values of 8–10°.

The results presented in Fig. 13a and b suggest that there are misorientations between dendrites or between regions which contain a few dendrites. The OM micrographs presented in Fig. 13c and d were taken parallel to the solidification direction (perpendicular to Fig. 13a and b). Primary dendrites which solidify in the [001] direction can be clearly distinguished. A closer look at the two images confirms the EBSD results presented in Fig. 13a and b. In Fig. 13c (taken close to x_S = 20 mm), two dendrites which extend over the whole image are marked by white dashed tracer lines. These two lines appear to be

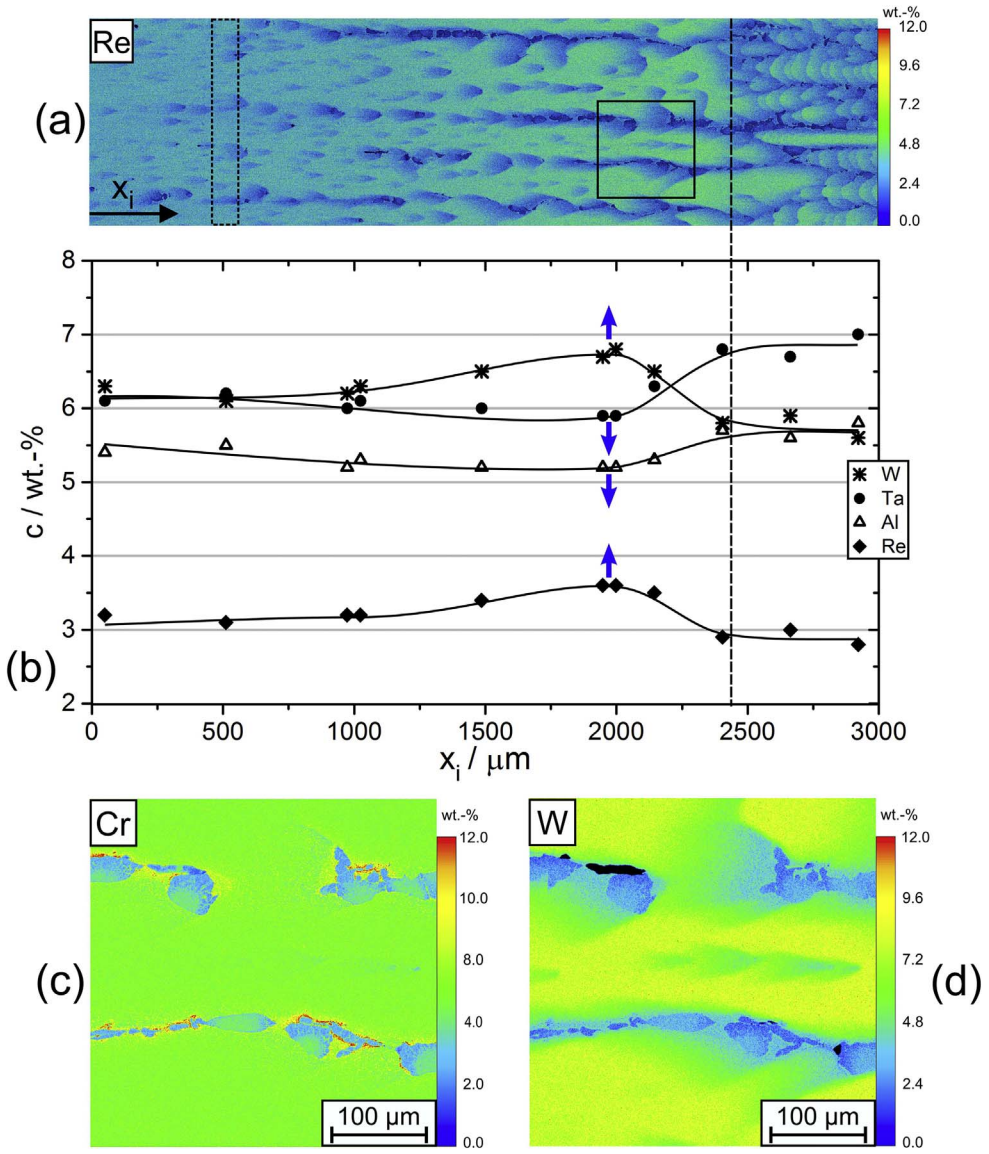

Fig. 7. Results from electron probe microanalysis (EPMA) obtained from the interface region between the back-melted seed and the newly grown crystal. (a) Re partitioning (micro scale between dendritic and interdendritic) and segregation (mm scale along solidified bar). (b) Concentration profiles of W, Ta, Al and Re in the region shown in Fig. 7a. (c) and (d) Color-coded distribution maps of Cr and W as observed in the square highlighted in Fig. 7a. For details see text.

parallel but a closer look reveals that they run in a projected angle of 2.3° with respect to each other. We expect that the two dendrites are separated by a LAGB which accounts for this angle. As we move close to the end of the new SX bar, deviations become more pronounced. In Fig. 13d four positions were chosen which allow to appreciate this increase of crystallographic deviations. At position 1 two dendrites which are parallel to each other are highlighted. As one follows these two dendrites in solidification direction, one finds that the secondary dendrites gradually disappear. This indicates that the two dendrites are slightly inclined with respect to the macroscopic solidification direction. At position 2 we find another dendrite, which clearly does not have the same direction as the two shown at position 1. At position 3, this dendrite branches into two. Both, the original and the new dendrite grow in parallel towards the end of the image. The dendrite marked with 4 in the upper part of the image seems to be more strongly inclined. This can be concluded because its secondary dendrites periodically appear and disappear as we move along the dendrite.

4. Discussion

4.1. Bridgman seed technique (BST)

In the present work we use a Bridgman technique with a seed crystal, Fig. 1. The seed crystal partially melts, Fig. 6a. Its remaining solid part provides a starting point for epitaxial growth of the new SX which forms during solidification when the furnace is removed at a rate of 180 mm/h, while the cylindrical Al_2O_3 mold (inner diameter: 12 mm, containing: spacer, seed crystal and feedstock, Fig. 1) remains fixed. It is well known that the temperature gradient across the solid/liquid interface is of crucial importance. Therefore numerous efforts were made to calculate temperature fields analytically (e.g. [56,57]) and numerically (e.g. [58,59]). Typical results reported in the literature range from 1 to 15 K/mm [4,7,28,43,54,60,61]. For the present setup and assuming quasistatic conditions we calculate a value of 14 K/mm using the WinCast Expert FEM software [48]. We obtain the thermal gradient by a linear fit of the temperature profile, Fig. 5b, between T_L and T_S. Table 4 lists different values for T_L and T_S for CMSX-4, which were compiled from the literature [49,62–64]. In addition, Table 4 contains one data triple for T_L, T_S, and $T_{S\text{-Scheil}}$ obtained using the

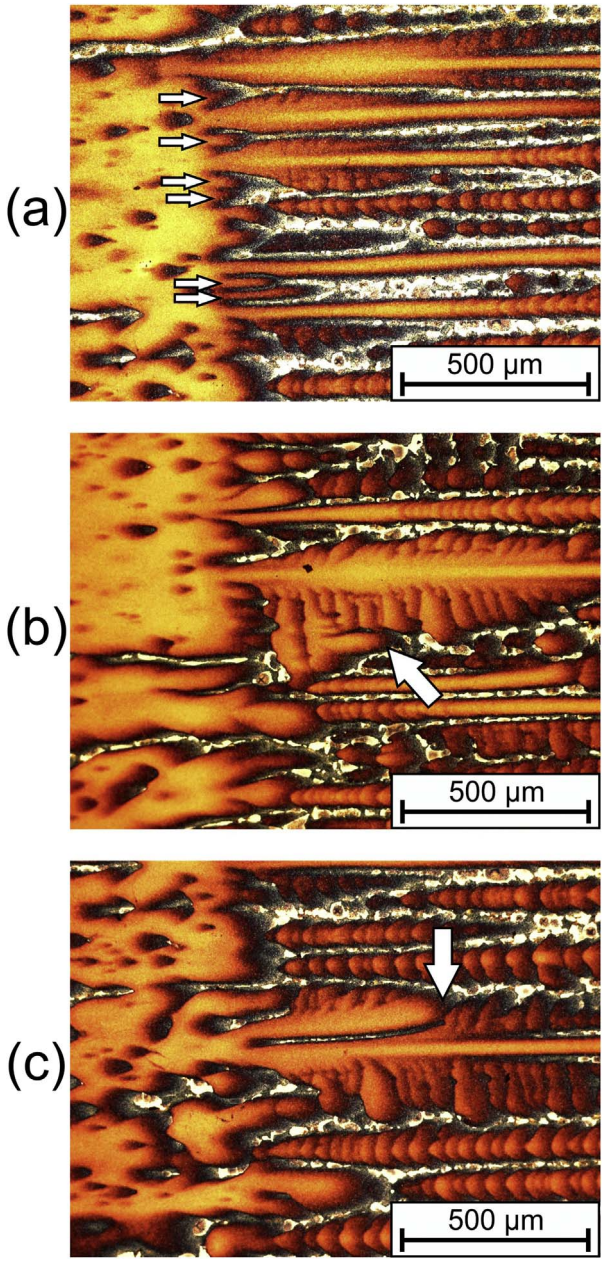

Fig. 8. Growth of dendrites from the seed/melt interface. (a) Formation of small protrusions (highlighted by arrows) between larger dendrites. (b) Formation of secondary and tertiary dendrites. The growth of one tertiary dendrite (highlighted by arrow) was stopped by secondary dendrites. (c) Competitive growth of two primary dendrites. The arrow highlights the position where the lower dendrite successfully outgrew its upper neighbor.

software Thermo-Calc and the thermodynamic database TCNI8 [65]. In this case, T_L and T_S correspond to equilibrium temperatures, whereas $T_{S\text{-Scheil}}$ represents a technical solidus temperature where compositional changes in the solid phase during solidification are excluded. $T_{S\text{-Scheil}}$ was assessed using the Scheil-equation [66] as implemented in Thermo-Calc. Fig. 14 shows the positions of the different characteristic temperatures listed in Table 4 as isothermal lines in a color-coded temperature distribution map. The region shown in Fig. 14 contains the lower part of the crucible and parts of the baffle. All characteristic isotherms are located above the baffle. Therefore, one can conclude that solidification in our BST process occurs above the upper side of the baffle. The mushy zone, i.e. the region between T_L and T_S, extends over ≈ 4 mm. Fig. 14 and Table 4 show that different authors report very similar T_L and T_S. We note that our calculated T_S-value represents a theoretical equilibrium temperature, which cannot be observed or measured in a technical solidification process. However, the calculated $T_{S\text{-Scheil}}$ temperature is close to the T_S data reported in literature [49,62–64]. The last column of Table 4 lists values of the thermal gradient G which was assessed by using the different T_L and T_S (respectively $T_{S\text{-Scheil}}$) values. Our study yields thermal gradients between 11.1 and 14 K/mm.

The thermal gradients of our BST process obtained by numerical simulation are in excellent agreement with an estimate which one can make based on the equation suggested by Fisher and Kurz [19],

$$\lambda_1 = k \cdot G^{\alpha} \cdot v^{\beta} \tag{1}$$

where λ_1 is the average primary dendrite arm spacing in μm, G represents the temperature gradient (unit: K/m) with an exponent α of − 1/2 and v is the withdrawal rate (m/s) with an exponent β of − 1/4 and k is a constant. Recently Matache et al. [54] have reported a value for the constant k for CMSX-4 type alloys as $1865.4 \cdot 10^{-6}\ m^{(3/4)} \cdot K^{(1/2)} \cdot s^{(-1/4)}$. With an average dendrite spacing of 205 μm from Fig. 10, this allows us to estimate a G of 11.7 K/mm. This value, derived from the microstructure (Eq. (1)) is in good agreement with the FEM data, Table. 4. Fig. 15 shows, that the average primary dendrite spacing which was determined in the present work is also in good agreement with literature data [31,60,67,68], which were compiled by Whitesell et al. [31] for various Ni-base superalloys, with additional data point for CMSX-4 from Matache et al. [54]. As has been outlined in the present work, our BST procedure allows to reproducibly process SX cylinders as shown in Fig. 2b. The size of these cylindrical crystals is small enough to establish homogenous temperature fields during melting and to allow for inexpensive parametric studies while their volumes are sufficiently large to take out miniature creep specimens of the type described by Wollgramm et al. [40].

4.2. Interface between seed and new SX

The results obtained in the present work show that the seed crystal partially melts, Fig. 6a. A mushy zone evolves at the interface between the seed and the new SX. A high quality optical micrograph of this zone is shown in Fig. 6d. The presence of mushy zones in back-melted seed regions was reported for CMSX-4 solidification in the literature [61,69–71]. CMSX-4 has a relatively large solidification interval [49,62,64]. The seed material used in the present work was an as-cast material state with a large average dendrite spacing close to 450 μm, Fig. 6b. It seems reasonable to assume that a seed material with better microstructural/chemical homogeneity will result in a narrower mushy zone and a smaller deviation from ideal dendrite growth directions. Fig. 7 compiles some interesting new results which were obtained in the region where the seed crystal was partially remelted. Remelting and the subsequent resolidification are associated with significant differences in local alloy composition. There are differences between prior dendritic and prior interdendritic seed regions, which extend over distances of the order of the primary dendrite arm spacing (a few hundred micrometers). Re and W partition to the prior dendrite cores, while Al and Ta partition to prior interdendritic regions. It must be kept in mind that this region of our system is kept for longer times (30 min) at a temperature where it is semi solid. This allows for large scale interdiffusion in the mushy zone. The small scale heterogeneities which we observe in Fig. 7a, c and d are associated with the resolidification of this mushy zone.

There are also long range concentration profiles which extend over several mm distances along the longitudinal direction of the bar, Fig. 7b. At higher temperatures, the molten material can solve more W and Re ($k' > 1$, [9,23,54]). As a consequence, W and Re diffuse to the right in Fig. 7b, i.e. towards the hotter regions of the melt, where T_L increases. The original degree of overheating required for melting decreases and this stabilizes the solid phase (constitutive cooling of the

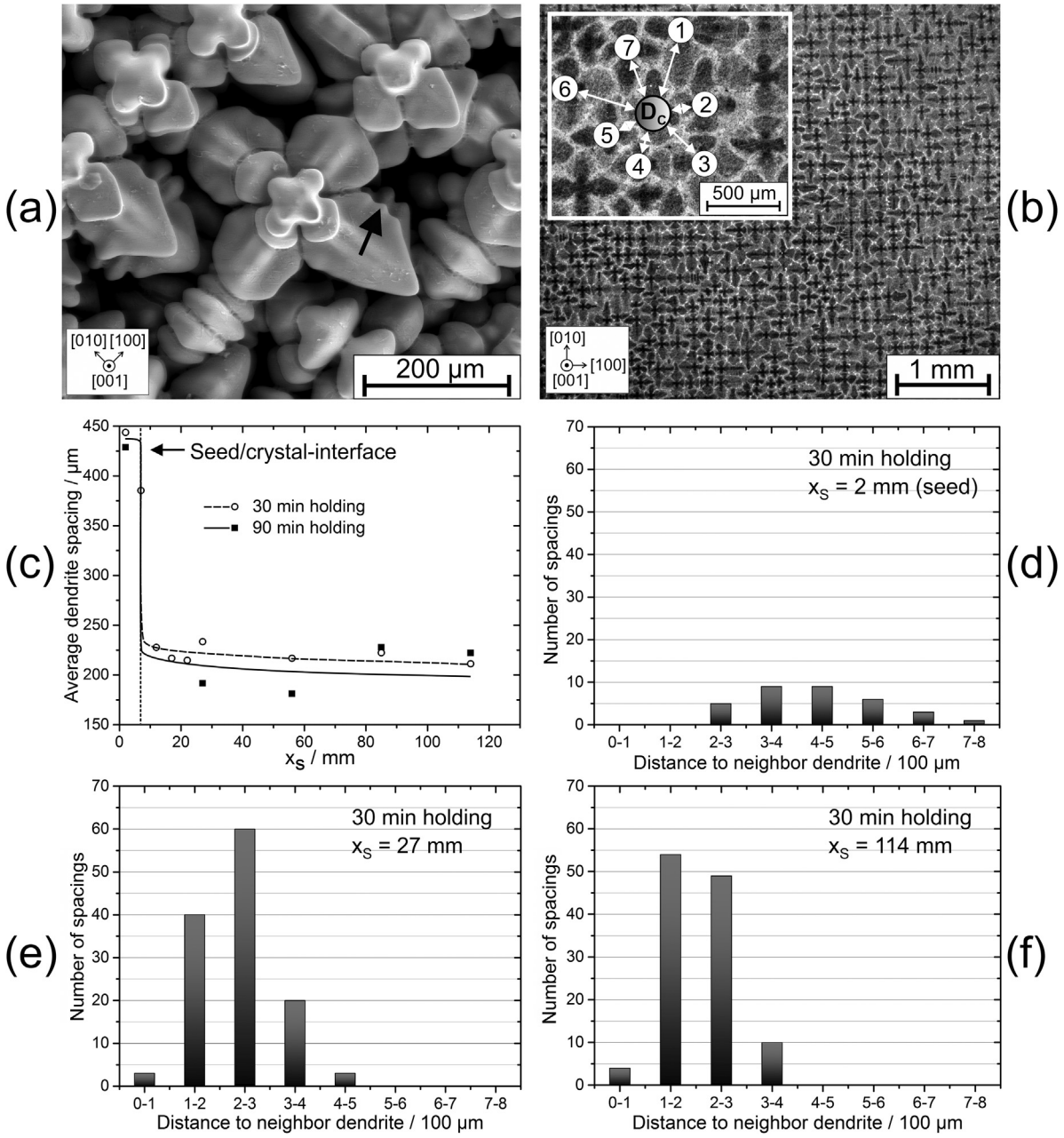

Fig. 9. Microstructure evolution during SX solidification. (a) SEM micrograph showing free-standing dendrites at the very end of the solidified bar. (b) Optical micrograph with dendrites taken from a cross section perpendicular to the growth direction. The inset exemplarily shows distances between one central dendrite D_C and its seven neighbors. (c) Two data sets (holding times: 30 and 90 min) showing how average primary dendrite arm spacings vary with x_S (as specified in Fig. 2c). (d, e and f) Histograms showing the distribution of dendrite arm spacings for different longitudinal bar positions x_S (for a 30 min holding time).

melt). The opposite holds for Al and Ta, which diffuse to colder zones (left part of Fig. 7b), where, as a consequence T_L decreases. Here the local overheating increases (constitutive heating of the melt). Where the mushy zone emerges from the fully solid seed crystal, melting appears to be promoted. On the other side of the mushy zone, the redistribution of elements stabilizes the solid phase. The seed seems to fight melting on the hot side of the mushy zone, on the expense of melting further in its colder parts. It also seems to be surprising that a system which shows so strong chemical heterogeneities can solidify as a single crystal and the question arises whether these heterogeneities are at the very heart of defect creation in SX.

The small protrusions shown in Fig. 8a show a striking resemblance to what was reported in the literature for an organic model system (see for example Fig. 24 of [72]). Due to constitutional undercooling, a flat interface is not stable [17,19,20]. The evolution of this type of morphology during casting can be well rationalized using phase field modeling [73,74]. The microstructural details shown in Fig. 8 suggest that not all protrusions evolve into full dendrites. This is related to the competitive growth and the underlying elementary selection processes, e.g. [19,72–75]. Only dendrites, with a large enough distance from competing dendrites, survive. When competitive growth has established the dendrite spacing enforced by the solidification conditions, stable growth is observed, Eq. (1).

4.3. Appearance of small randomly oriented grains

Only one of the five SX crystals processed in the present work contained two relatively small (1 mm) randomly oriented grains in the melt-back zone of the seed, close to the mushy zone, Fig. 12. Stanford et al. [69] reported similar microstructural features. They related their findings to the pinching

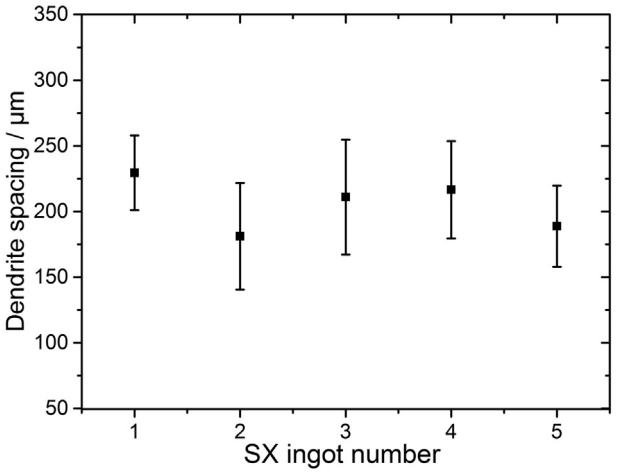

Fig. 10. Primary dendrite arm spacings (with error bars) at x_S = 56 mm in five cylindrical SX bars produced with the BST process.

off of dendrite fragments. Neither in the study of Stanford et al. [69] nor in the present work it was observed, that this type of defect gives rise to the growth of larger misoriented regions. Regularly solidifying dendrites appear to have better growth conditions [76] and the size of these defects is therefore kept at a minimum. Even though it has been reported in the literature that Bridgman processing with seed crystals can give rise to the formation of stray grains [53,61,69,70,77,78], no stray grains were detected in the present work. As an example, Fig. 1a in reference [70] shows that stray grains form in surface regions during seeded DS casting. They are known to form close to the perimeter of the seed close to the mold wall. Stanford et al. [70] suggest that these defects can survive competitive dendrite growth for concave solid/liquid interfaces. Zhou et al. [53] describe a blocking mechanism, which allows misaligned stray grains to overgrow favorably oriented, regular grains. The stray grains represent one of the reasons why commercial seeded directional SX solidification is often performed in combination with a crystal selector [61,70,77]. Our procedure seems to be less prone to stray grain formation than approaches, where the superalloy melt is poured into a mold which contains a colder seed crystal [61,70,77]. In our case, seed and melting feedstock are in direct contact throughout the whole processing cycle, where they melt simultaneously. Casting convection in the melt may have an influence, and it may cause flotation of pinched-off or leached-off dendrite fragments [36,79,80] which later evolve into larger grains. Most probably, the non-convective nature of our technique in combination with our small melt volume hamper these processes.

4.4. Low angle grain boundaries, mosaicity, chemical homogeneity

The results presented in Fig. 13 show that our material contains small angle boundaries. These can be easily detected using orientation imaging SEM, Fig. 13a and b. The presence of these small angle grain boundaries on cross sections which were taken perpendicular to the solidification direction, is directly related to the growth directions of primary dendrites, Fig. 13c. On cross sections which are parallel to the axis of the cylindrical specimen, small misorientations between this targeted growth direction and the actual growth direction of a dendrite also become apparent, when it is observed that secondary dendrite arms seem to appear and disappear as one moves along the dendrite axis. The small deviations from ideal primary dendrite growth directions are responsible for the mosaicity which is apparent in Fig. 13a and b [55,81,82]. Mosaicity which accompanies dendritic solidification has been observed in Ni-base superalloys on several occasions and typical misorientation angles of the order of 2° were reported [28,43,83], in agreement with what we find in Fig. 13b. Bogdanowicz et al. [28] studied this phenomenon using X-ray diffraction. They come to the conclusion that new dendrite branching events introduce additional misorientations. D'Souza et al. [43] investigated this phenomenon by EBSD in an as-cast superalloy turbine blade. They observed an increase of misorientation angles when dendrite growth deviated from the original solidification direction. They suggested that this phenomenon is related to deformation of dendrites driven by thermal and (less likely) convection-related stresses. Dendrite bending and torsion were experimentally observed by Aveson et al. [84] during in-situ synchrotron solidification experiments. Many of the complexities briefly discussed in this section do not necessarily play a role in our system. There clearly is pre-existing mosaicity in our seed crystal which the newly forming crystal inherits. But as the micrographs presented in Fig. 13c and d suggest, the degree of mosaicity evolves towards a higher spread as directional solidification proceeds. This may be related to additional deformation of dendrites, which is caused by thermal or shrinkage stresses as reported in [84–88]. Further work is required to study this phenomenon and to optimize processing conditions with the objective to keep crystal mosaicity at a minimum.

4.5. Homogeneity and reproducibility of processing route

The results presented in Figs. 11a and b show that our cylindrical bars show a good chemical homogeneity. This proves that the method

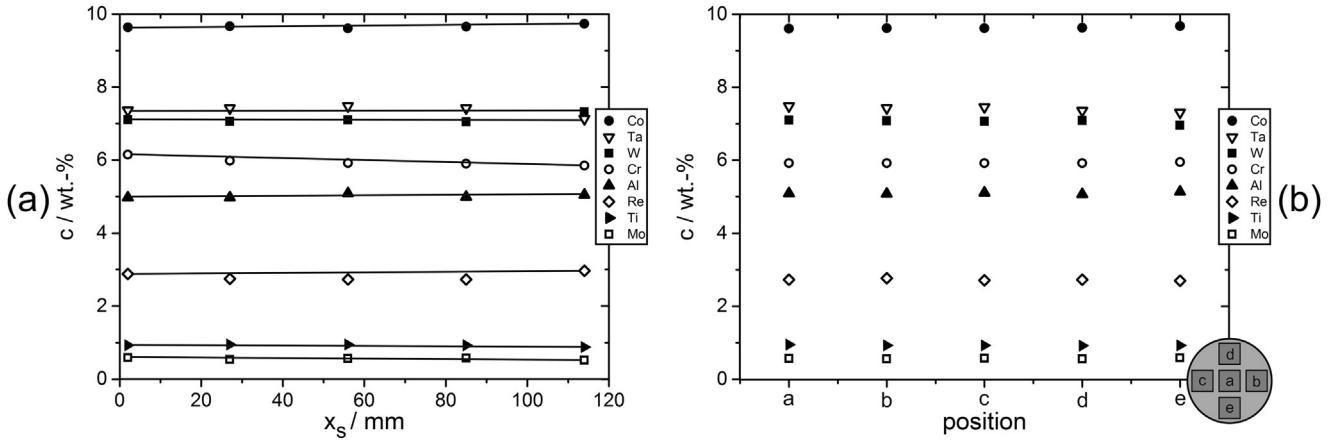

Fig. 11. Chemical homogeneity of cylindrical SX bars. (a) Variation of concentrations of alloy elements along the cylinder axis. (b) Variation of concentrations in different cross sectional regions. For details see text.

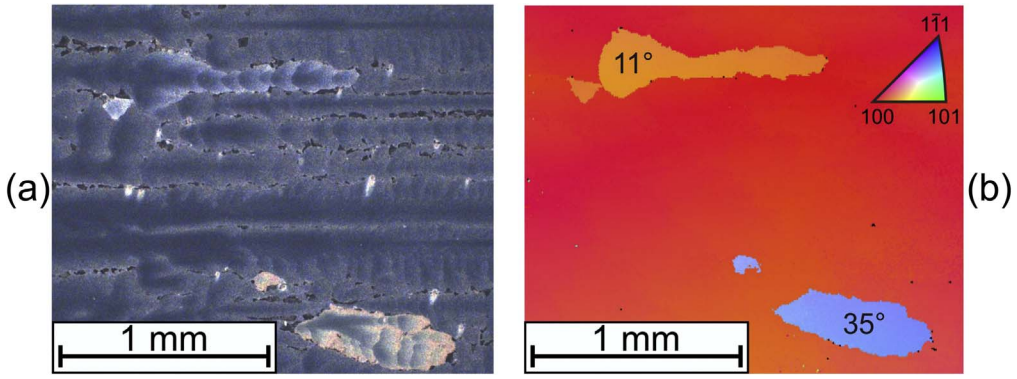

Fig. 12. Detection of rare grain defects. (a) Optical micrograph. (b) EBSD/OIM data confirming significant deviations in crystal orientations (IPF-ND map, see inset with color coding). Grain defects were only observed in the transitional zone between the mushy zone of the seed and the newly formed crystal in one out of 5 samples.

which we document in the present work can provide chemically homogenous samples even in the case of an alloy like CMSX-4 which has a strong partitioning tendency, e.g. [6]. Moreover, the results shown in Fig. 10 show that very similar microstructural features are established in five SX ingots which were solidified under the same conditions. This shows that the method yields reproducible SX material.

5. Summary and conclusions

In the present work we use a Bridgman seed technique (BST, withdrawal rate v: 180 mm/h, temperature gradient G across liquid/solid interface region: 14 K/mm) to cast cylindrical ingots (length: 120 mm, diameter: 12 mm) of a single crystal (SX) Ni-base superalloy. A number of open questions were studied which address the evolution of local alloy chemistry and microstructure in the technical single crystal. From the results obtained in the present work, the following conclusions can be drawn:

(1) When using a BST method, the seed crystal melts partially. A mushy zone develops between the remaining seed and the melt. In the semi liquid state, a specific type of segregation results in constitutive cooling/heating on the hot/cold side of the mushy zone where it

Table 4
Compilation of liquidus and solidus temperatures for CMSX-4 and derived thermal gradients G for the BST procedure applied in the present work.

	T_L/K	T_S/K	$T_{S\text{-}Scheil}$/K	Remark	G/(K/mm)
Quested et al. [49]	1653	1593	–	Experimental	13.9
Aune et al. [62]	1655	1585	–	Experimental	14
Matsushita et al. [63]	1680	1655	–	Calculated	11.1
Szczotok et al. [64]	1658/1654	1599/1591	–	Exp. heating/cooling	13.7/13.9
Present work	1655	1613	1587	Calculated	13.3

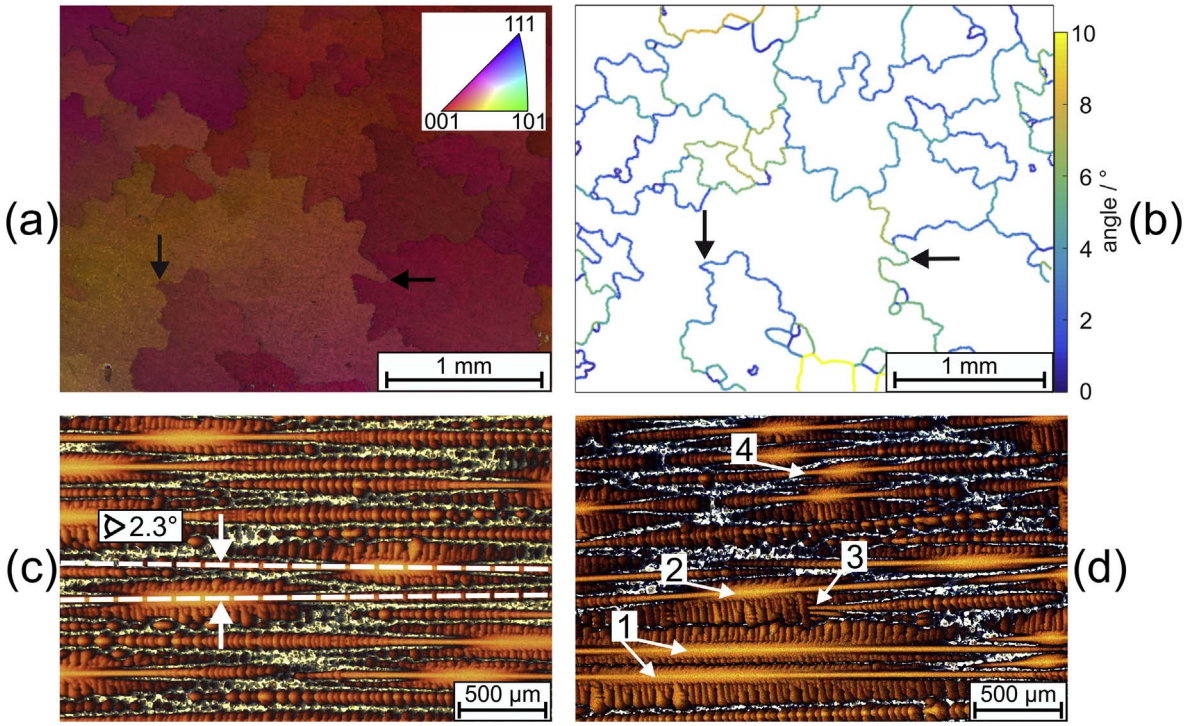

Fig. 13. Crystal mosaicity in as-grown superalloy samples. (a) EBSD/OIM data (IPF-ND, cross section sample) with superimposed image quality map showing regions with slightly different orientations. (b) Distribution of misorientation angles (values given in degree). (c) Optical micrograph obtained from longitudinal sections showing misoriented dendrites at $x_S \approx 20$ mm. (d) Same type of microstructure at $x_S \approx 116$ mm. For details see text.

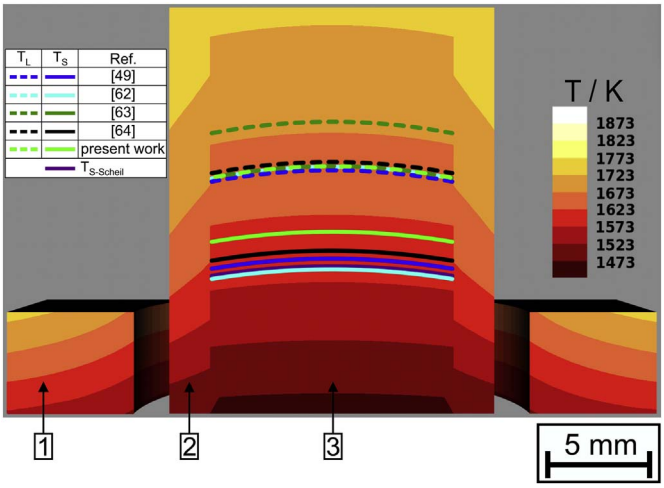

Fig. 14. Comparison of the positions of liquidus and solidus isotherms in the crucible resulting from different solidification temperatures obtained from literature [49,62–64] and the present work, see Table 4. Arrows indicate 1 - baffle, 2 - crucible tube, and 3 - feedstock.

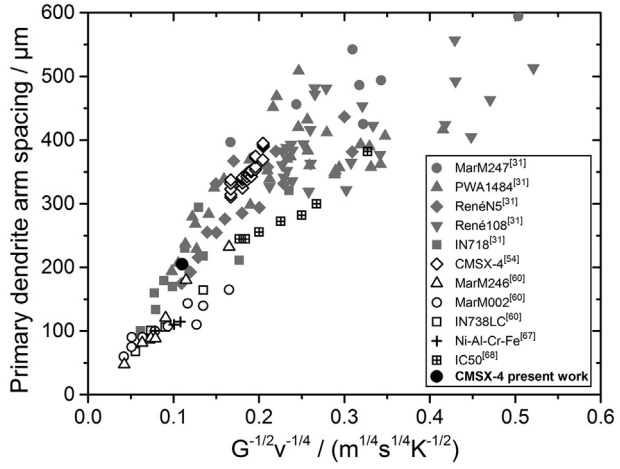

Fig. 15. Literature data for the dependence of primary dendrite arm spacings on thermal gradients (G) and solidification rates (v) for various Ni-based superalloys (taken from [31], with additional data points from [54]). The full circular symbol represents the result obtained in the present work.

stabilizes/destabilizes the solid phase.

(2) The elementary microstructural evolution processes which govern solidification in the early stages of crystal growth were characterized. Competitive growth can interrupt the formation of primary dendrites which evolve from small protrusions which emanate from the seed crystal. Branching events, where new primary dendrites originate from secondary dendrite arms were observed. Competitive growth eventually establishes a constant average dendrite spacing across the specimen length.

(3) The calculated temperature gradient of 14 K/mm, which was obtained using a numerical FEM procedure is in excellent agreement with an experimental gradient which can be obtained from the Kurz-Fisher equation, using the experimental withdrawal rate and the microstructurally determined average dendrite spacing.

(4) The presence of small angle grain boundaries on cross sections which were taken perpendicular to the solidification direction could be directly traced back to deviations from the ideal growth directions of primary dendrites. An effort was made to identify misorientation angles of low angle grain boundaries using EBSD/OIM. Misorientation angles were typically close to 2°, only occasionally higher deviations of up to 8° were observed.

(5) The present work provides information on microstructural scatter associated with the processing of five individual SX ingots. The five ingots show very similar primary dendrite spacings. Only in one of five ingots two little (1 mm) grains were found which likely are associated with the back melting of the seed crystal and the break out of seed dendrite segments.

Acknowledgement

The authors acknowledge funding by the Deutsche Forschungsgemeinschaft (DFG) through projects B7 and C5 of the collaborative research center SFB/TR 103 on single crystal superalloys (see: www.sfb-transregio103.de). The authors also appreciate advice and helpful discussions with Katarzyna Matuszewska and Ralf Rettig (Friedrich-Alexander-University Erlangen-Nürnberg) on single crystal growing. The authors also appreciate help from RWP GmbH for their assistance with the FEM calculations.

References

[1] F.I. Versnyder, M.E. Shank, The development of columnar grain and single crystal high temperature materials through directional solidification, Mater. Sci. Eng. 6 (4) (1970) 213–247.
[2] G.W. Meetham, The Development of Gas Turbine Materials, Applied Science Publishers, London, 1981.
[3] M. McLean, Directionally Solidified Materials for High Temperature Service, The Metals Society, London, 1983.
[4] D. Goldschmidt, Einkristalline Gasturbinenschaufeln aus Nickelbasis-Legierungen. Teil I: Herstellung und Mikrogefüge, Materialwiss. Werkst. Techn. 25 (8) (1994) 311–320.
[5] D. Goldschmidt, Einkristalline Gasturbinenschaufeln aus Nickelbasis-Legierungen. Teil II: Wärmebehandlung und Eigenschaften, Materialwiss. Werkst. Techn. 25 (9) (1994) 373–382.
[6] R.C. Reed, Single-crystal superalloys for blade application, in: R.C. Reed (Ed.), The Superalloys — Fundamentals and Applications, Cambridge Univ. Press, Cambridge, 2006, pp. 121–147.
[7] R. Bürgel, H.J. Maier, T. Niendorf, Hochtemperaturlegierungen, in: R. Bürgel, H.J. Maier, T. Niendorf (Eds.), Handbuch Hochtemperatur-Werkstofftechnik, Vieweg + Teubner Verlag, Wiesbaden, 2011, pp. 340–484.
[8] T.M. Pollock, S. Tin, Nickel-based superalloys for advanced turbine engines: chemistry, microstructure and properties, J. Propuls. Power 22 (2) (2006) 361–374.
[9] A.B. Parsa, P. Wollgramm, H. Buck, C. Somsen, A. Kostka, I. Povstugar, P.P. Choi, D. Raabe, A. Dlouhy, J. Müller, E. Spiecker, K. Demtröder, J. Schreuer, K. Neuking, G. Eggeler, Advanced scale bridging microstructure analysis of single crystal Ni-Base superalloys, Adv. Eng. Mater. 17 (2) (2015) 216–230.
[10] P. Carter, D.C. Cox, C.A. Gandin, R.C. Reed, Process modelling of grain selection during the solidification of single crystal superalloy castings, Mater. Sci. Eng. A 280 (2) (2000) 233–246.
[11] K. Demtröder, G. Eggeler, J. Schreuer, Influence of microstructure on macroscopic elastic properties and thermal expansion of nickel-base superalloys ERBO/1 and LEK94, Materialwiss. Werkst. Techn. 46 (6) (2015) 563–576.
[12] P.E. Aba-Perea, T. Pirling, P.J. Withers, J. Kelleher, S. Kabra, M. Preuss, Determination of the high temperature elastic properties and diffraction elastic constants of Ni-base superalloys, Mater. Des. 89 (2016) 856–863.
[13] K. Kubiak, D. Szeliga, J. Sieniawski, A. Onyszko, The unidirectional crystallization of metals and alloys (turbine blades), in: P. Rudolph (Ed.), Handbook of Crystal Growth (Second Edition) — Bulk Crystal Growth: Growth Mechanisms and Dynamics, Elsevier, Amsterdam, 2015.
[14] J.J. Gilman, The Art and Science of Growing Crystals, John Wiley & Sons, New York, 1963.
[15] G. Dhanaraj, K. Byrappa, V. Prasad, M. Dudley, Crystal growth techniques and characterization: an overview, in: G. Dhanaraj, K. Byrappa, V. Prasad, M. Dudley (Eds.), Springer Handbook of Crystal Growth, Springer, Berlin, 2010, pp. 3–16.
[16] J.J. Derby, A. Yeckel, Heat transfer analysis and design for bulk crystal growth: perspectives of the Bridgman method, in: P. Rudolph (Ed.), Handbook of Crystal Growth (Second Edition) — Bulk Crystal Growth: Growth Mechanisms and Dynamics, Elsevier, Amsterdam, 2015, pp. 793–843.
[17] J.D. Hunt, Solidification and Casting of Metals, The Metals Society, London, 1979.
[18] K.A. Jackson, Kinetic Processes, Wiley-VCH, Weinheim, 2004.
[19] W.W. Kurz, D.J. Fisher, Fundamentals of Solidification, fourth ed., Trans Tech Publ. (2005) Aedermannsdorf.
[20] D.M. Stefanescu, Science and Engineering of Casting Solidification, second ed., Springer, New York, 2009.
[21] W.J. Boettinger, S.R. Coriell, A.L. Greer, A. Karma, W. Kurz, M. Rappaz, R. Trivedi, Solidification microstructures: recent developments, future directions, Acta Mater. 48 (1) (2000) 43–70.
[22] Q. Feng, T.K. Nandy, S. Tin, T.M. Pollock, Solidification of high-refractory ruthenium-containing superalloys, Acta Mater. 51 (1) (2003) 269–284.
[23] F. Wang, D.X. Ma, J. Zhang, A. Bührig-Polaczek, Investigation of segregation and density profiles in the mushy zone of CMSX-4 superalloys solidified during downward and upward directional solidification processes, J. Alloys Compd. 620

(2015) 24–30.
[24] N. D'Souza, M.G. Ardakani, A. Wagner, B.A. Shollock, M. McLean, Morphological aspects of competitive grain growth during directional solidification of a nickel-base superalloy, CMSX4, J. Mater. Sci. 37 (3) (2002) 481–487.
[25] T.M. Pollock, W.H. Murphy, The breakdown of single-crystal solidification in high refractory nickel-base alloys, Metal. Mater. Trans. A 27 (4) (1996) 1081–1094.
[26] R.A. Hobbs, S. Tin, C.M.F. Rae, A castability model based on elemental solid-liquid partitioning in advanced nickel-base single-crystal superalloys, Metall. Mater. Trans. A 36A (10) (2005) 2761–2773.
[27] F. Wang, D.X. Ma, Y.R. Mao, S. Bogner, A. Bührig-Polaczek, Influence of the size effect on the microstructures of the DWDS- and Bridgman-solidified single-crystal CMSX-4 superalloy, Metall. Mater. Trans. B Process Metall. Mater. Process. Sci. 47 (1) (2016) 76–84.
[28] W. Bogdanowicz, R. Albrecht, J. Sieniawski, K. Kubiak, The subgrain structure in turbine blade roots of CMSX-4 superalloy, J. Cryst. Growth 401 (2014) 418–422.
[29] W. Kossel, Zur Theorie des Kristallwachstums, Nachrichten von der Gesellschaft der Wissenschaften zu Göttingen, Mathematisch-Physikalische Klasse (1927) 135–143.
[30] I.N. Stranski, Zur Theorie des Kristallwachstums, Z. Phys. Chem. 1356 (1928) 259–278.
[31] H.S. Whitesell, L. Li, R.A. Overfelt, Influence of solidification variables on the dendrite arm spacings of Ni-based superalloys, Metall. Mater. Trans. B 31 (3) (2000) 546–551.
[32] S.S. Babu, M.K. Miller, J.M. Vitek, S.A. David, Characterization of the microstructure evolution in a nickel base superalloy during continuous cooling conditions, Acta Mater. 49 (20) (2001) 4149–4160.
[33] N. D'Souza, H.B. Dong, Solidification path in third-generation Ni-based superalloys, with an emphasis on last stage solidification, Scr. Mater. 56 (1) (2007) 41–44.
[34] I. Lopez-Galilea, S. Huth, S.G. Fries, N. Warnken, I. Steinbach, W. Theisen, Microsegregation and secondary phase formation during directional solidification of the single-crystal Ni-based superalloy LEK94, Metall. Mater. Trans. A 43A (13) (2012) 5153–5164.
[35] M.C. Schneider, J.P. Gu, C. Beckermann, W.J. Boettinger, U.R. Kattner, Modeling of micro- and macrosegregation and freckle formation in single-crystal nickel-base superalloy directional solidification, Metall. Mater. Trans. A 28 (7) (1997) 1517–1531.
[36] J.P. Gu, C. Beckermann, A.F. Giamei, Motion and remelting of dendrite fragments during directional solidification of a nickel-base superalloy, Metall. Mater. Trans. A 28 (7) (1997) 1533–1542.
[37] L. Qin, J. Shen, G. Yang, Q. Li, Z. Shang, A design of non-uniform thickness mould for controlling temperature gradient and S/L interface shape in directionally solidified superalloy blade, Mater. Des. 116 (2017) 565–576.
[38] M. Rahimian, S. Milenkovic, L. Maestro, A. Eguidazu Ruiz De Azua, I. Sabirov, Development of tool for physical simulation of skin formation during investment casting of nickel-based superalloys, Mater. Des. 87 (2015) 712–720.
[39] K. Hoshikawa, J. Osada, Y. Saitou, E. Ohba, C. Miyagawa, T. Kobayashi, J. Yanagisawa, M. Shinozuka, K. Kanno, Vertical Bridgman growth of sapphire — seed crystal shapes and seeding characteristics, J. Cryst. Growth 395 (2014) 80–89.
[40] P. Wollgramm, D. Bürger, A.B. Parsa, K. Neuking, G. Eggeler, The effect of stress, temperature and loading direction on the creep behaviour of Ni-base single crystal superalloy miniature tensile specimens, Mater. High Temp. 33 (4–5) (2016) 346–360.
[41] J. Frenzel, E.P. George, A. Dlouhy, C. Somsen, M.F.X. Wagner, G. Eggeler, Influence of Ni on martensitic phase transformations in NiTi shape memory alloys, Acta Mater. 58 (9) (2010) 3444–3458.
[42] M. Rahim, J. Frenzel, M. Frotscher, J. Pfetzing-Micklich, R. Steegmüller, M. Wohlschlögel, H. Mughrabi, G. Eggeler, Impurity levels and fatigue lives of pseudoelastic NiTi shape memory alloys, Acta Mater. 61 (10) (2013) 3667–3686.
[43] N. D'Souza, M. Newell, K. Devendra, P.A. Jennings, M.G. Ardakani, B.A. Shollock, Formation of low angle boundaries in Ni-based superalloys, Mater. Sci. Eng. A 413 (2005) 567–570.
[44] C. Merlet, An accurate computer correction program for quantitative electron-probe microanalysis, Mikrochim. Acta 114 (1994) 363–376.
[45] F. Bachmann, R. Hielscher, H. Schaeben, Grain detection from 2d and 3d EBSD data — specification of the MTEX algorithm, Ultramicroscopy 111 (12) (2011) 1720–1733.
[46] F. Bachmann, R. Hielscher, P.E. Jupp, W. Pantleon, H. Schaeben, E. Wegert, Inferential statistics of electron backscatter diffraction data from within individual crystalline grains, J. Appl. Crystallogr. 43 (2010) 1338–1355.
[47] O. Engler, V. Randle, Introduction to Texture Analysis — Macrotexture, Microtexture, and Orientation Mapping, second ed., CRC Press, Boca Raton, 2010.
[48] RWP GmbH, http://www.rwp-simtec.de/home.html, Roetgen, Germany, 2016.
[49] P.N. Quested, R.F. Brooks, L. Chapman, R. Morrell, Y. Youssef, K.C. Mills, Measurement and estimation of thermophysical properties of nickel based superalloys, Mater. Sci. Technol. 25 (2) (2009) 154–162.
[50] M.W. Chase Jr., NIST-JANAF Thermochemical Tables, Monograph No.9, 4th ed., NIST1998.
[51] S. Picard, D.T. Burns, P. Roger, Measurement of the Specific Heat Capacity of Graphite, Rapport BIPM-2006/01, International Bureau of Weights and Measures, France, 2006.
[52] Material Data Sheets From Furnace Component Manufacturers, (2016).
[53] Y.Z. Zhou, A. Volek, N.R. Green, Mechanism of competitive grain growth in directional solidification of a nickel-base superalloy, Acta Mater. 56 (11) (2008) 2631–2637.
[54] G. Matache, D.M. Stefanescu, C. Puscasu, E. Alexandrescu, Dendritic segregation and arm spacing in directionally solidified CMSX-4 superalloy, Int. J. Cast. Metal. Res. (2016) 303–316.
[55] C.G. Darwin XCII, The reflexion of X-rays from imperfect crystals, Phil. Mag. Series 6 43(257) (1922) 800–829.
[56] C.E. Chang, W.R. Wilcox, Control of interface shape in the vertical Bridgman-Stockbarger technique, J. Cryst. Growth 21 (1) (1974) 135–140.
[57] S. Sen, W.R. Wilcox, Influence of crucible on interface shape, position and sensitivity in the vertical Bridgman-Stockbarger technique, J. Cryst. Growth 28 (1) (1975) 36–40.
[58] H. Miyazawa, L. Liu, K. Kakimoto, Numerical analysis of influence of crucible shape on interface shape in a unidirectional solidification process, J. Cryst. Growth 310 (6) (2008) 1142–1147.
[59] C. Stelian, Numerical modeling of radiative heat transfer in Bridgman solidification of semi-transparent BaF_2 crystals, J. Cryst. Growth 306 (2) (2007) 444–451.
[60] P.N. Quested, M. McLean, Solidification morphologies in directionally solidified superalloys, Mater. Sci. Eng. 65 (1) (1984) 171–180.
[61] N. D'Souza, P.A. Jennings, X.L. Yang, P.D. Lee, M. McLean, H.B. Dong, Seeding of single-crystal superalloys — role of constitutional undercooling and primary dendrite orientation on stray-grain nucleation and growth, Metall. Mater. Trans. B 36 (5) (2005) 657–666.
[62] R.E. Aune, L. Battezzati, R. Brooks, I. Egry, H.J. Fecht, J.P. Garandet, M. Hayashi, K.C. Mills, A. Passerone, P.N. Quested, E. Ricci, F. Schmidt-Hohagen, S. Seetharaman, B. Vinet, R.K. Wunderlich, Thermophysical properties of IN738lc, MM247lc and CMSX-4 in the liquid and high temperature solid phase, in: E.A. Loria (Ed.), Superalloys 718, 625, 706 and Derivatives, Minerals, Metals & Materials Soc. 2005, pp. 467–476 Warrendale.
[63] T. Matsushita, H.J. Fecht, R.K. Wunderlich, I. Egry, S. Seetharaman, Studies of the thermophysical properties of commercial CMSX-4 alloy, J. Chem. Eng. Data 54 (9) (2009) 2584–2592.
[64] A. Szczotok, R. Przeliorz, Phase Transformations in CMSX-4 Nickel-Base Superalloy, Technologies and Properties of Modern Utilised Materials, Iop Publishing Ltd., Bristol, 2012.
[65] Thermo-Calc, http://www.thermocalc.com, Stockholm, Sweden.
[66] E. Scheil, Bemerkungen zur Schichtkristasllbildung, Z. Metallkd. 34 (1942) 70–72.
[67] M. Vijayakumar, S.N. Tewari, J.E. Lee, P.A. Curreri, Dendrite spacings in directionally solidified superalloy PWA-1480, Mater. Sci. Eng. A 132 (1991) 195–201.
[68] D.M. Wang, unpublished work reported in [31].
[69] N. Stanford, A. Djakovic, B.A. Shollock, M. McLean, N. D'Souza, P.A. Jennings, Seeding of single crystal superalloys — role of seed melt-back on casting defects, Scr. Mater. 50 (1) (2004) 159–163.
[70] N. Stanford, A. Djakovic, B. Shollock, M. McLean, N. D'Souza, P. Jennings, Defect Grains in the Melt-back Region of CMSX-4 Single Crystal Seeds, Minerals, Metals & Materials Soc. (2004) Warrendale.
[71] G.S. Chen, P.R. Aimone, M. Gao, C.D. Miller, R.P. Wei, Growth of nickel-base superalloy bicrystals by the seeding technique with a modified Bridgman method, J. Cryst. Growth 179 (3–4) (1997) 635–646.
[72] J.D. Hunt, S.Z. Lu, Numerical modeling of cellular/dendritic array growth: spacing and structure predictions, Metal. Mater. Trans. A 27 (3) (1996) 611–623.
[73] I. Steinbach, Effect of interface anisotropy on spacing selection in constrained dendrite growth, Acta Mater. 56 (18) (2008) 4965–4971.
[74] Z. Wang, J. Li, J. Wang, Y. Zhou, Phase field modeling the selection mechanism of primary dendritic spacing in directional solidification, Acta Mater. 60 (5) (2012) 1957–1964.
[75] B.J. Spencer, H.E. Huppert, The relationship between dendrite tip characteristics and dendrite spacings in alloy directional solidification, J. Cryst. Growth 200 (1–2) (1999) 287–296.
[76] D. Walton, B. Chalmers, The origin of the preferred orientation in the columnar zone of ingots, Trans. Am. I. Min. Met. Eng. 215 (3) (1959) 447–457.
[77] Y.Z. Zhou, Formation of stray grains during directional solidification of a nickel-based superalloy, Scr. Mater. 65 (4) (2011) 281–284.
[78] C. Yang, L. Liu, X. Zhao, J. Zhang, D. Sun, H. Fu, Formation of stray grains during directional solidification of a superalloy AM3, Appl. Phys. A Mater. Sci. Process. 114 (3) (2013) 979–983.
[79] S. Liu, S.-Z. Lu, A. Hellawell, Dendritic array growth in the systems NH_4Cl–H_2O and $[CH_2\ CN]_2$–H_2O: the detachment of dendrite side arms induced by deceleration, J. Cryst. Growth 234 (4) (2002) 740–750.
[80] K.A. Jackson, J.D. Hunt, D.R. Uhlmann, T.P. Seward, On origin of equiaxed zone in castings, Trans. Metall. Soc. AIME 236 (2) (1966) 149–158.
[81] J.R. Schneider, H.A. Graf, High resolution studies of crystal mosaicity by means of double crystal γ-ray diffractometry, J. Cryst. Growth 74 (1) (1986) 191–202.
[82] M. Deutsch, M. Hart, S. Cummings, How perfect is a perfect crystal? Part-per-billion level mosaicity measurements in silicon, Appl. Phys. Lett. 51 (18) (1987) 1410–1412.
[83] U. Brückner, A. Epishin, T. Link, Local X-ray diffraction analysis of the structure of dendrites in single-crystal nickel-base superalloys, Acta Mater. 45 (12) (1997) 5223–5231.
[84] J.W. Aveson, G. Reinhart, H. Nguyen-Thi, N. Mangelinck-Noël, A. Tandjaoui, B. Billia, K. Goodwin, T.A. Lafford, J. Baruchel, H.J. Stone, N. D'Souza, Dendrite Bending during Directional Solidification, Superalloys 2012, John Wiley & Sons, Inc., Hoboken, 2012, pp. 615–624.
[85] R.D. Doherty, Comments on "Mechanical deformation of dendrites by fluid flow during the solidification of undercooled melts", Scr. Mater. 49 (12) (2003) 1219–1222.
[86] T. Uehara, T. Tsujino, Phase field simulation of stress evolution during solidification, J. Cryst. Growth 275 (1–2) (2005) e219–e224.
[87] T. Uehara, M. Fukui, N. Ohno, Phase field simulations of stress distributions in solidification structures, J. Cryst. Growth 310 (7–9) (2008) 1331–1336.
[88] M. Yamaguchi, C. Beckermann, Simulation of solid deformation during solidification: compression of a single dendrite, Acta Mater. 61 (11) (2013) 4053–4065.